



## Construction of AgBiO<sub>3</sub>/g-C<sub>3</sub>N<sub>4</sub> nanocomposites with enhanced photocatalytic activity and their application in the degradation of bisphenol A

Zehua Zhao<sup>a,†</sup>, Yi Wang<sup>a,†</sup>, Qiang Yu<sup>b</sup>, Xiaochen Lin<sup>a</sup>, Xiaowei Xu<sup>a</sup>, Jun Zhang<sup>a</sup>, Haijun Lu<sup>a</sup>, Xiaoxi Chen<sup>a</sup>, Dapeng Zhang<sup>a,\*</sup>

<sup>a</sup>Nanjing Institute of Environmental Sciences, Ministry of Ecology and Environment of the People's Republic of China, 8 Jiangwangmiao Street, Nanjing 210042, China, email: hazhangdapeng@163.com (D. Zhang)

<sup>b</sup>Solid Waste Management Center, Department of Ecology and Environment of Jiangxi Province, 1131 Hongdu North Street, 330077, China

Received 4 January 2021; Accepted 3 April 2021

### ABSTRACT

In this paper, AgBiO<sub>3</sub> and g-C<sub>3</sub>N<sub>4</sub> materials were prepared by the ion-exchange method and calcination method, respectively. Their composite materials with different compositions were prepared by changing the dosage of raw materials during the synthetic process. The prepared nanocomposite materials were utilized to degrade bisphenol A (BPA) under visible light irradiation. By comparison, 50 wt.% AgBiO<sub>3</sub> in AgBiO<sub>3</sub>/g-C<sub>3</sub>N<sub>4</sub> (ABC-50) owns the supreme photocatalytic activity with 95.75% degradation efficiency of BPA and the degradation process was proven to follow the pseudo-first-order kinetics. In addition, the oxidative species of <sup>•</sup>O<sub>2</sub> and h<sup>+</sup> and OH were found to play equal roles in the photocatalytic reaction process.

**Keywords:** g-C<sub>3</sub>N<sub>4</sub>; AgBiO<sub>3</sub>; Bisphenol A; Photocatalyst; Nanocomposite

### 1. Introduction

Bisphenol A (BPA) is one of the common organic compounds with two phenol moieties. It has significant properties such as low vapor pressure, moderate water solubility, and low volatility. BPA has been widely used to produce polymer materials such as polycarbonates, epoxy, and polysulfone resins [1]. The frequent and unorganized emission of BPA into the natural environment at low concentrations has aroused people and the government's great attention. It has been detected in soil, rivers and atmosphere in multiple countries and regions [2]. As a kind of common endocrine disruptors, BPA could affect nerve cell damage that can lead to the abnormal or disruptive behavior of humans and cause thyroid dysfunction [3,4]. Besides, previous work reported that the higher concentration of BPA (over 30 μM)

can hamper plant growth by invigorating the reaction oxygen species and lipid peroxidation in Arabidopsis [5]. Hence, it is urgent to find simple, cost-effective and efficient treatment methods to handle the trouble of BPA pollution. Some treatment methods like the physical method [6,7], the biological method [8,9] and the chemical method [10,11] have been reported before.

As a kind of environmentally friendly technology, the photocatalytic process has shown excellent performance in catalytic degradation of organic pollutants. As known, it is key for the process to find suitable photocatalytic semiconductors [12–14]. It is commonly thought that TiO<sub>2</sub> was firstly used as a photocatalyst for generating hydrogen by Fujishima and Honda in 1972 [15]. Whereafter, plenty of semiconductors such as CdS, ZnO, and Bi<sub>2</sub>WO<sub>6</sub> have been employed for photocatalytic reaction. But most of these

\* Corresponding author.

† These authors contributed equally to this work.

photocatalytic materials are uneconomical and poor visible light absorbance [16]. In recent years, the successful preparation of graphitic phase carbon nitride ( $g\text{-C}_3\text{N}_4$ ) and its remarkable performance in the field of photocatalysis have aroused wide interest among scholars.  $g\text{-C}_3\text{N}_4$  is a typical, metal-free, polymeric, novel semiconductor material with a bandgap of about 2.7 eV and can absorb visible light [17–20]. However, it's a central issue for  $g\text{-C}_3\text{N}_4$  to improve the separation efficiency between holes ( $h^+$ ) and electron ( $e^-$ ) and the utilization efficiency of visible light, due to its wide bandgap, high recombination efficiency of photogenic carriers and low light utilization efficiency [21–23]. Some modifications have been often employed, including semiconductor coupling [24–26], metal doping [27,28], non-metal doping [29,30] and dye sensitization [31,32].

Bismuthates are considered as attractive perovskite materials owing to the stabilization in their exclusive electric structure of  $\text{MBiO}_3$  ( $M=\text{Na, Li, Ag}$ ) [33]. Bismuth element with two valences ( $\text{Bi}^{5+}$  and  $\text{Bi}^{3+}$ ) exists in the twisty octahedral ( $\text{BiO}_6$ ) structure [34,35]. The excellent oxidizability is exhibited due to the empty 6s band of  $\text{Bi}^{5+}$  and the filled 6s band of  $\text{Bi}^{3+}$  [36]. As a kind of  $\text{MBiO}_3$  material,  $\text{AgBiO}_3$  not only has the outstanding properties above but also owns excellent visible light absorption performance and effective bacteriostatic ability. It has been successfully applied to the control of water blooms [37,38]. In this paper, a simple and fast growth method was employed to synthesize  $\text{AgBiO}_3/g\text{-C}_3\text{N}_4$  photocatalytic materials. The physico-chemical properties of the synthesized  $\text{AgBiO}_3/g\text{-C}_3\text{N}_4$  have been characterized. It exhibits an enhanced photocatalytic activity for the removal of BPA under visible light. Furthermore, the possible mechanism for the photodegradation process of  $\text{AgBiO}_3/g\text{-C}_3\text{N}_4$  was speculated.

## 2. Experimental

### 2.1. Chemicals

Melamine and BPA were purchased from Sinopharm Chemical Reagent Company (Shanghai, China). Analytical grade silver nitrate, sodium hydroxide, sulfuric acid, sodium bismuthate, sodium chloride, absolute ethyl alcohol, p-benzoquinone, isopropanol, potassium iodide were obtained from Shanghai Chemical Reagent Company (Shanghai, China). Purified water (Wahaha Group Co., Ltd., Hangzhou, China) was used throughout the experiments. All chemicals were used without further purification.

### 2.2. Apparatus

Transmission electron microscopy (TEM, JEM-200CX microscope, JEOL, Tokyo, Japan), scanning electron microscope (SEM, Hitachi S-4800, Tokyo, Japan) and energy dispersive X-ray spectrometry (EDX, EX250, Horiba, Kyoto, Japan) were employed to observe the morphology and the structure of  $g\text{-C}_3\text{N}_4$ ,  $\text{AgBiO}_3$  and  $\text{AgBiO}_3/g\text{-C}_3\text{N}_4$  nanomaterials. Fourier-transform infrared spectroscopy (FT-IR) was recorded on a TENSOR 27 spectrometer using a potassium bromide pellet (Bruker, Saarbrücken, Germany). The phase purity and crystallinity of the as-prepared materials were identified by X-ray powder diffraction (XRD)

patterns on a Rigaku XRD-6000 diffractometer with a  $\text{Cu K}\alpha$  radiation ( $\lambda = 0.15406$  nm) (Shimadzu, Kyoto, Japan). X-ray photoelectron spectroscopy (XPS) data was performed on an Escalab 250Xi instrument (Thermo, USA). The ultraviolet-visible diffuse reflectance spectroscopy (UV-Vis DRS) was characterized with a Cary 5000 spectrophotometer in the 200–800 nm range and  $\text{BaSO}_4$  was chosen as the reference (Varian, USA). Photoluminescence (PL) analysis was performed by a Cary Eclipse spectrophotometer (Varian, USA). The Brunauer–Emmett–Teller (BET) surface area test was performed on a TRISTAR-3000 surface area analyzer.

### 2.3. Preparation of the photocatalytic materials

#### 2.3.1. Preparation of $g\text{-C}_3\text{N}_4$

The  $g\text{-C}_3\text{N}_4$  nanosheets were synthesized by the pyrolysis method with minor modifications [39]. 20 g melamine was calcining in a muffle furnace at  $520^\circ\text{C}$  for 4 h under air atmosphere. The yellow solid obtained is  $g\text{-C}_3\text{N}_4$ .

#### 2.3.2. Preparation of $\text{AgBiO}_3$

The  $\text{AgBiO}_3$  was prepared by the ion-exchange method [33]. In brief, 2.8 g  $\text{NaBiO}_3$  was dispersed in 100 mL of water with continuous stirring at  $30^\circ\text{C}$  for 60 min. Then, 100 mL  $0.1$  mol  $\text{L}^{-1}$   $\text{AgNO}_3$  solution was slowly added into the mixture above. After keeping stirring for 24 h, the suspension was filtered and washed alternately with anhydrous ethanol and deionized water 2–3 times.  $\text{AgBiO}_3$  was obtained after drying at low temperature for 6 h.

#### 2.3.3. Preparation of $\text{AgBiO}_3/g\text{-C}_3\text{N}_4$ nanocomposites

The preparation process of  $\text{AgBiO}_3/g\text{-C}_3\text{N}_4$  nanocomposites is similar to that of  $\text{AgBiO}_3$ . A certain amount of  $g\text{-C}_3\text{N}_4$  and  $\text{NaBiO}_3$  were dispersed in 60 mL mixed solvent ( $V_{\text{ethanol}}:V_{\text{water}} = 1:2$ ) with continuing ultrasonication for 30 min. Then,  $0.1$  mol  $\text{L}^{-1}$   $\text{AgNO}_3$  solution was slowly added into the mixture above. After reaction for 24 h, the suspension was filtered and washed alternately with ethanol and deionized water 2–3 times. In the experiments, different mass percentages of  $\text{AgBiO}_3$  (66%, 50% and 33%) in  $\text{AgBiO}_3/g\text{-C}_3\text{N}_4$  composite materials were obtained by changing the dosing of  $g\text{-C}_3\text{N}_4$  and they were labeled ABC-66, ABC-50 and ABC-33, respectively.

## 3. Results and discussion

### 3.1. Characterization of the prepared materials

#### 3.1.1. Morphology analysis

Fig. 1a displays that single  $g\text{-C}_3\text{N}_4$  has a lamellar structure, which is similar to Lan et al. [18]. In Fig. 1b,  $\text{AgBiO}_3$  nanomaterial appears to own a spherical-like structure. Fig. 1c shows the prepared  $\text{AgBiO}_3$  aggregated seriously. Fig. 1d–f exhibits  $\text{AgBiO}_3$  is successfully loaded on the surface of  $g\text{-C}_3\text{N}_4$ . As shown in Fig. 1g, the lattice fringes of ABC-50 have a spacing of 0.23 nm, which is in accord with the spacing of the (202) planes of  $\text{AgBiO}_3$ . Fig. 1h reveals the elements C, N, O, Ag and Bi are all observed in the ABC-50.

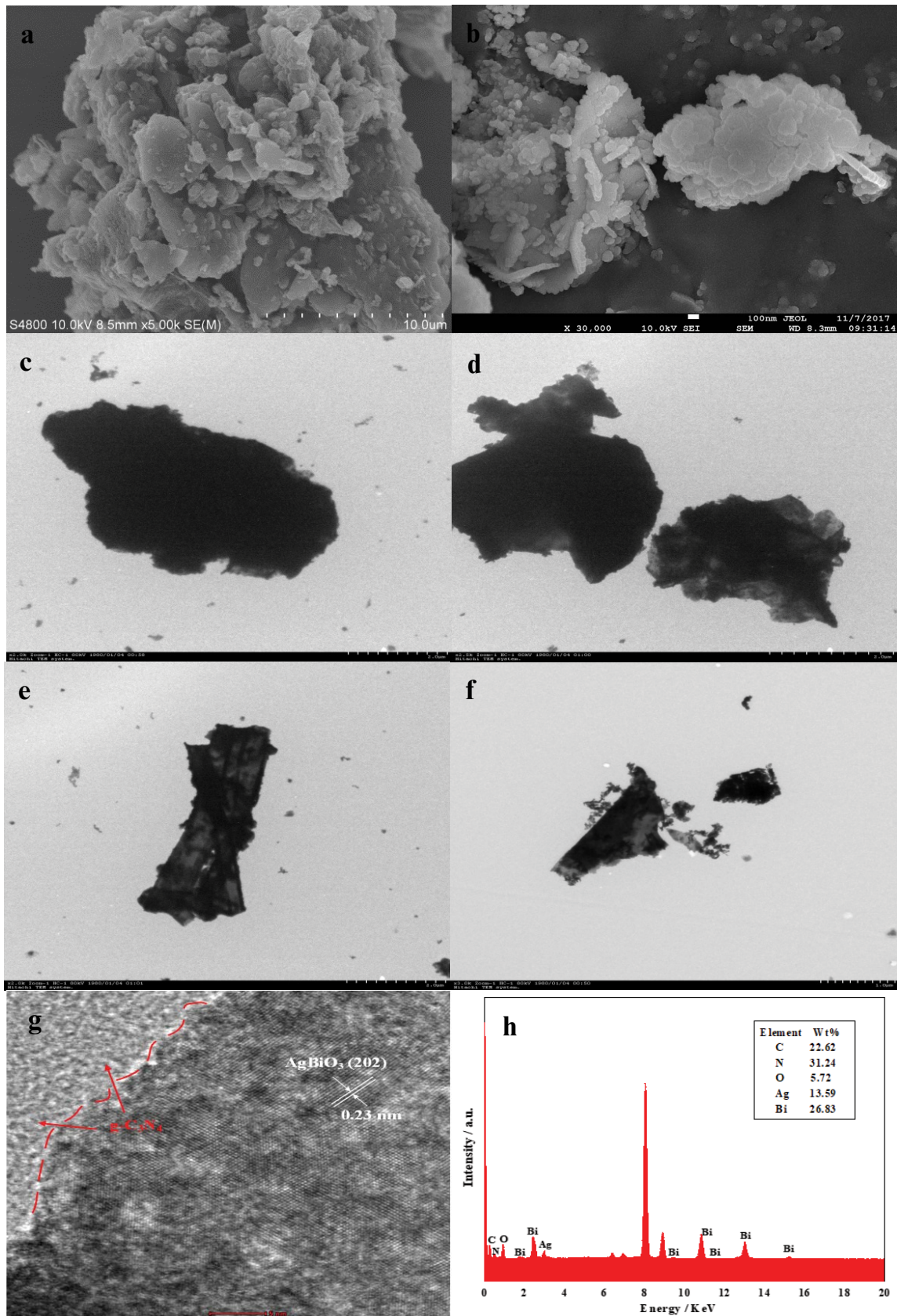


Fig. 1. SEM images of  $g\text{-C}_3\text{N}_4$  (a) and  $\text{AgBiO}_3$  (b); TEM images of  $\text{AgBiO}_3$  (c), ABC-66 (d), ABC-50 (e), ABC-33 (f); high-resolution transmission electron microscopy (HRTEM) of ABC-50 (g); EDX image of ABC-50 (h).

The mass ratio of the C element is slightly more than the theoretical value. It may result from the existence of CO<sub>2</sub> in the atmosphere.

### 3.1.2. FT-IR analysis

As shown in Fig. 2a, the peaks of 1,639 and 1,250 cm<sup>-1</sup> are attributed to the stretching vibration of C=N and C–N [39], respectively. The wide peaks at 3,100–3,400 cm<sup>-1</sup> correspond to the –NH<sub>2</sub> group [25]. The peak of 809 cm<sup>-1</sup> results from the breathing of the triazine units of g-C<sub>3</sub>N<sub>4</sub> [40]. The characteristic peak at 446 cm<sup>-1</sup> is assigned to the stretching vibration of Bi–O in AgBiO<sub>3</sub> (Fig. 2b) [41]. All the typical peaks of g-C<sub>3</sub>N<sub>4</sub> and AgBiO<sub>3</sub> are contained in the binary ABC composites (Fig. 2c–e), which shows the successful preparation of the composite materials.

### 3.1.3. XRD analysis

XRD was used to analyze the crystal structures of g-C<sub>3</sub>N<sub>4</sub>, AgBiO<sub>3</sub> and the synthesized ABC composite materials. In Fig. 3a, the intense peaks at 13.15° and 27.50° are corresponding to the (100) and (002) planes, respectively, which results from the characteristic inter-planar stacking of the aromatic systems [42]. Fig. 3b reveals the characteristic diffraction peaks of AgBiO<sub>3</sub> are at 21.8°, 31.7°, 46.8° and 56.7°, respectively. These peaks are indexed as the (012), (110), (116) and (300) crystal planes of AgBiO<sub>3</sub> in JCPDS Card No. 89–9072 [41]. Fig. 3c–e shows the XRD patterns of in ABC composite materials with different components. An obvious peak at 38.5° can be observed on the curves, which might be caused by a small amount of NaBiO<sub>3</sub> particles remaining in the prepared samples. All the diffraction peaks of g-C<sub>3</sub>N<sub>4</sub> and AgBiO<sub>3</sub> can be seen in the composites, which exhibits the ABC nanocomposites are successfully synthesized.

### 3.1.4. XPS analysis

XPS was utilized to analyze the inner structure of ABC-50 nanomaterial. In the full scan spectrum (Fig. 4a),

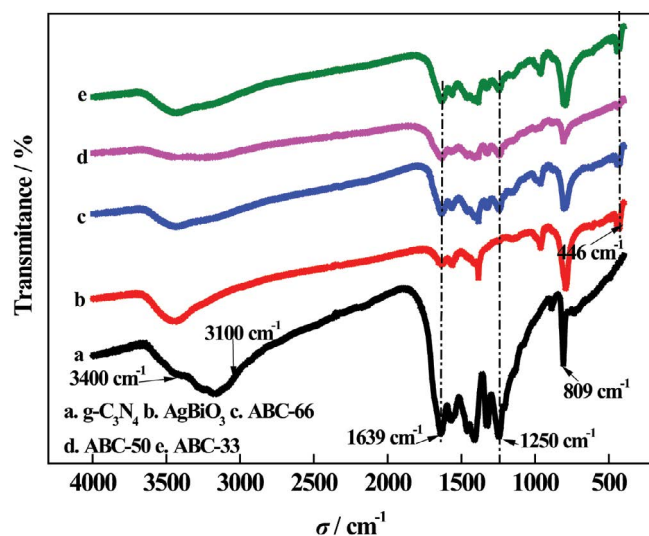


Fig. 2. FT-IR spectra of g-C<sub>3</sub>N<sub>4</sub> (a), AgBiO<sub>3</sub> (b), ABC-66 (c), ABC-50 (d) and ABC-33 (e).

the elements of C, N, O, Ag and Bi are contained in ABC-50 nanocomposite. In Fig. 4b, The C 1s peak at 284.3 eV is contributed to the C–C. The double peaks of 287.2 and 287.7 eV are assigned to C–(N)<sub>3</sub> [25]. N 1s spectrum (Fig. 4c) exhibits that the peak of 397.7 eV is ascribed to the bonds of C=N–C, and the peaks at 398.5 and 401.0 eV result from C–N–H and N–(C)<sub>3</sub> [43], which demonstrates the presence of g-C<sub>3</sub>N<sub>4</sub> in ABC-50. As shown in Fig. 4d, the binding energy of O 1s owns three characteristic peaks at 529.4, 530.6 and 531.7 eV, indicating the existence of lattice oxygen, active oxygen or chemisorbed oxygen, and adsorbed oxygen, respectively [41,44–46]. Fig. 4e shows the spectrum of Ag 3d. The binding energies of Ag 3d<sub>5/2</sub> and Ag 3d<sub>3/2</sub> have the typical peaks at 365.6 and 371.6 eV, respectively, with ΔE = 6 eV, which verifies the existence of Ag<sup>+</sup> in AgBiO<sub>3</sub> [36,38]. The double intense peaks at 161.7 and 156.4 eV result from the binding energies of Bi 4f<sub>5/2</sub> and Bi 2p<sub>7/2</sub> and which confirms the presence of Bi<sup>5+</sup> [36].

### 3.1.5. DRS analysis

In fact, the bandgap ( $E_g$ ) of AgBiO<sub>3</sub> is a controversial issue. Yu et al. [37] reported AgBiO<sub>3</sub> owns the bandgap of 2.5 eV, while of AgBiO<sub>3</sub> is 0.8 eV by DFT calculations in Ma's research [47]. Light absorption performance of catalytic materials plays a crucial role in photocatalytic activities. In this work, the UV-vis DRS spectra of g-C<sub>3</sub>N<sub>4</sub>, AgBiO<sub>3</sub> and ABC-50 nanocomposite are exhibited in Fig. 5a. The basic absorption edge of g-C<sub>3</sub>N<sub>4</sub> is approximately 460 nm, while the prepared AgBiO<sub>3</sub> has the basic absorption edge at 570 nm. Compared with the two materials, the ABC-50 composite has obvious absorption smears in the range of 450–800 nm. It is reported both AgBiO<sub>3</sub> and g-C<sub>3</sub>N<sub>4</sub> are indirect bandgap semiconductors [17,37]. The bandgaps of AgBiO<sub>3</sub> and g-C<sub>3</sub>N<sub>4</sub> can be calculated based on the classic Tauc approach Eq. (1).

$$\alpha h\nu = A(h\nu - E_g)^{n/2} \quad (1)$$

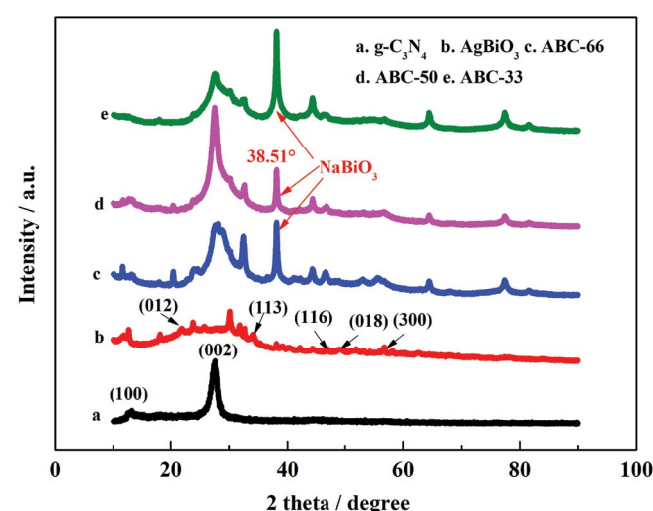


Fig. 3. XRD patterns of g-C<sub>3</sub>N<sub>4</sub> (a), AgBiO<sub>3</sub> (b), ABC-66 (c), ABC-50 (d) and ABC-33 (e).

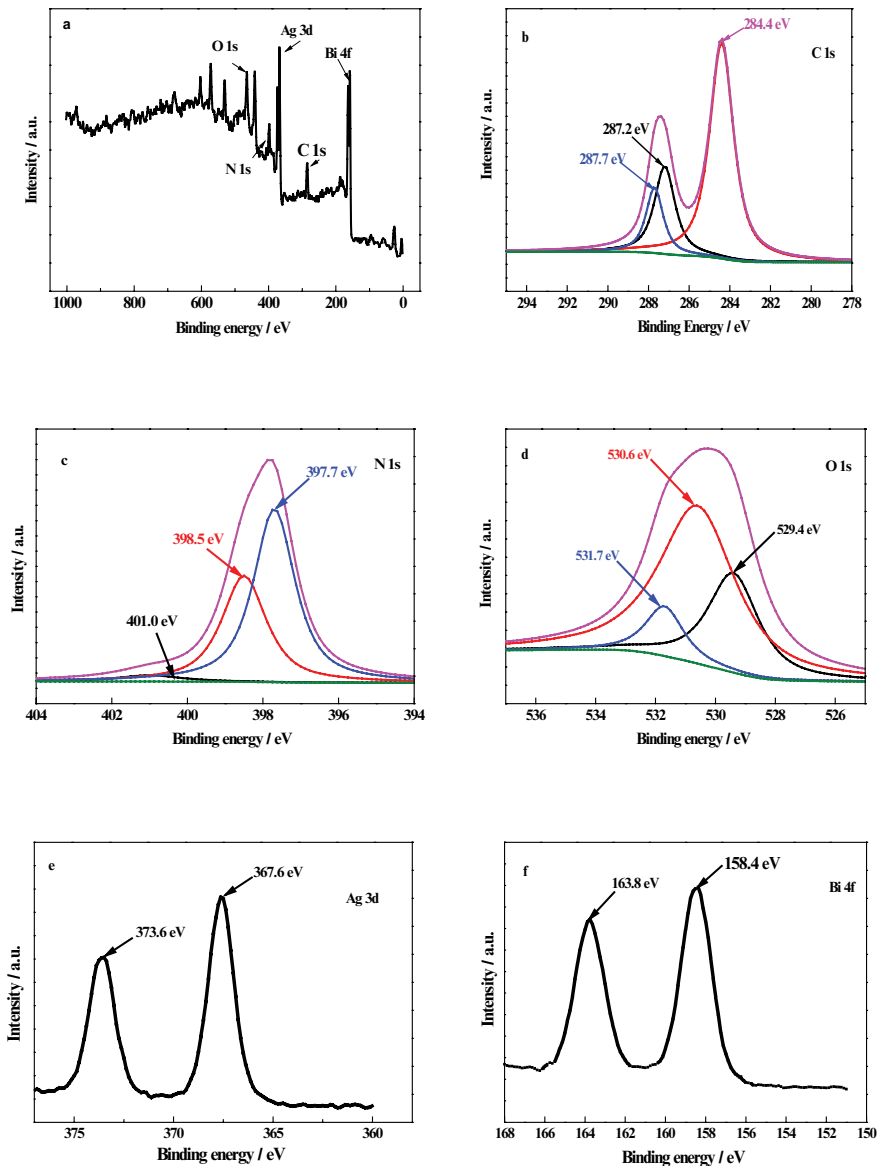


Fig. 4. The overview (a) and the corresponding high-resolution XPS spectra C 1s (b), N 1s (c), O 1s (d), Ag 3d (e) and Bi 4f (f) of the as-prepared ABC-50 nanomaterial.

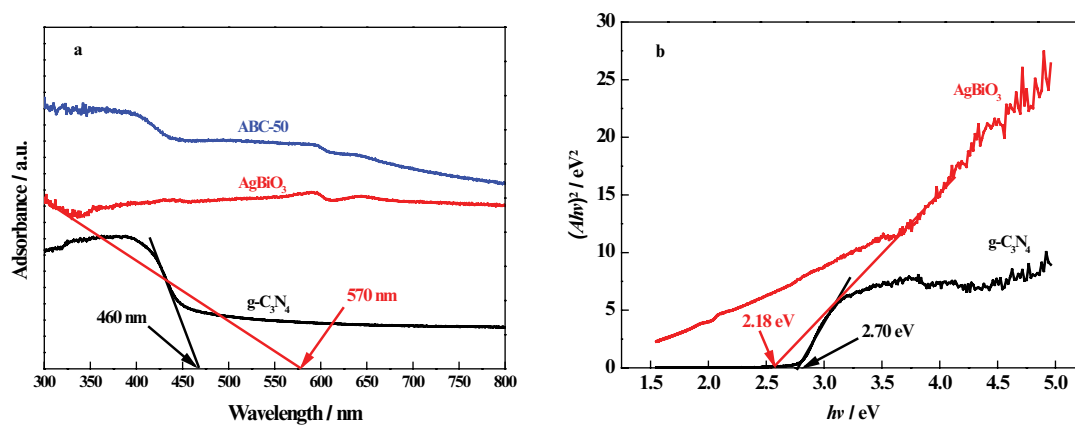


Fig. 5. DRS spectra of  $g\text{-C}_3\text{N}_4$ ,  $\text{AgBiO}_3$ , and ABC-50 nanocomposite.

where  $n$  is 4 for indirect transition and  $n$  is 1 for direct transition.  $\alpha$ ,  $h$ ,  $\nu$  and  $A$  are the absorption coefficient, Planck constant, light frequency and a constant, respectively [48]. Fig. 5b manifests the  $E_g$  of  $g\text{-C}_3\text{N}_4$  and  $\text{AgBiO}_3$  are at 2.70 and 2.18 eV, respectively.

### 3.1.6. PL analysis

In order to study the generation and separation of photogenic carriers in the prepared materials, fluorescence intensity was measured at an excitation wavelength of 325 nm.  $g\text{-C}_3\text{N}_4$  has a bandgap of 2.70 eV, which leads to a high probability of recombination between photogenic electrons and holes. As shown in Fig. 6, when  $\text{AgBiO}_3$  is introduced onto the surface of  $g\text{-C}_3\text{N}_4$ , the fluorescence emission intensity generated by ABC-50 is significantly lower than that generated by  $g\text{-C}_3\text{N}_4$ , which greatly enhances the utilization efficiency of visible light.

### 3.1.7. BET analysis

In Fig. 7, the BET specific surface area and pore size distribution of the prepared materials were investigated by  $\text{N}_2$  adsorption–desorption isotherm. The BET specific surface area of  $g\text{-C}_3\text{N}_4$ ,  $\text{AgBiO}_3$  and ABC-50 are 7.7638, 14.5080 and 32.1338  $\text{m}^2 \text{g}^{-1}$ , respectively. The pore diameter of ABC-50 is about 6.3–58.7 nm, which indicates ABC-50 nanomaterial is mesoporous. Larger surface area can provide more reaction sites, which is beneficial to the photocatalytic reaction process.

## 3.2. Photocatalytic degradation of BPA

### 3.2.1. Effect of the component ratio of $\text{AgBiO}_3/g\text{-C}_3\text{N}_4$ on the degradation of BPA

20 mg different photocatalytic materials were added into 50 mL 10 mg  $\text{L}^{-1}$  BPA solutions, respectively. Fig. 8 exhibits both  $g\text{-C}_3\text{N}_4$  and  $\text{AgBiO}_3$  have low degradation efficiency on BPA under 180 min visible light irradiation. Compared

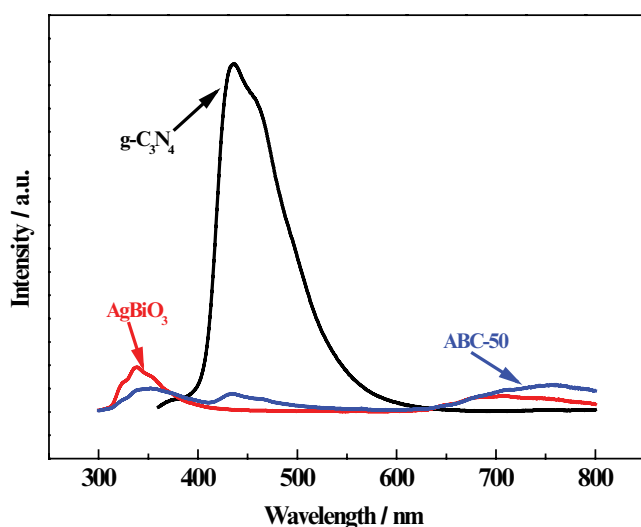


Fig. 6. PL spectra of  $g\text{-C}_3\text{N}_4$  (a),  $\text{AgBiO}_3$  (b) and ABC-50 (c).

with single catalysts, ABC nanocomposites display the obviously enhanced photocatalytic activity. When ABC-50 was used as the catalyst to degrade BPA, the removal efficiency can reach the highest. It results from the effective electrons migration from the ABC-50 nanocomposite. Hence, ABC-50 nanomaterial was used in the following experiments.

### 3.2.2. Effect of salinity on the degradation of BPA

As shown in Fig. 9, the removal efficiency of BPA decreases with the increase of NaCl concentration in the solution. When the dosage of NaCl was 0.9%, BPA degradation efficiency decreased to 67.20%. It may probably be concerned with the occupation of  $\text{Na}^+$  on the reactivity sites of the ABC-50 nanomaterial, which prohibits the BPA molecules from adsorbing onto the ABC-50 surface [49]. In addition, competitive adsorption among  $\text{Cl}^-$ ,  $\text{OH}^-$  and electrons would be formed on the surface of ABC-50.

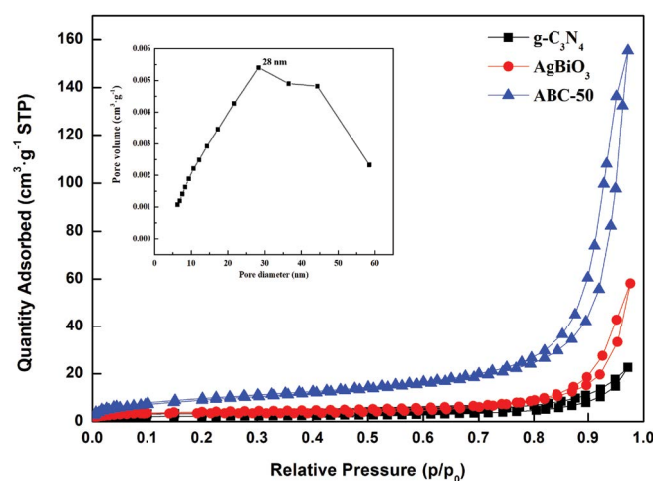


Fig. 7. Nitrogen adsorption–desorption isotherm plots for  $g\text{-C}_3\text{N}_4$ ,  $\text{AgBiO}_3$  and ABC-50 with the pore size distribution of ABC-50 in the left-top inset.

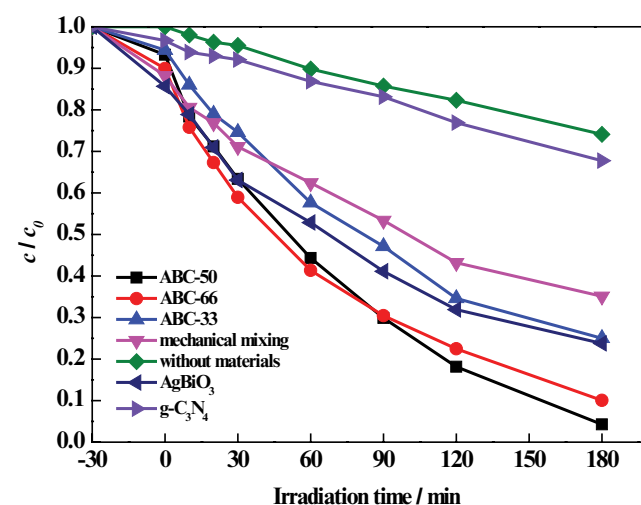


Fig. 8. Effect of the component ratio on the degradation efficiency of BPA.

Kinetics studies have been shown in Fig. 10. The reaction obeys the pseudo-first-order kinetics owing to the linear relationship between  $\ln(C_0/C)$  and reaction time [Eq. (2)].

$$\ln\left(\frac{C_0}{C}\right) = kt \quad (2)$$

where  $C_0$  is the initial concentration of BPA (units:  $\text{mg L}^{-1}$ ) and  $C$  is the concentration of BPA after the photocatalytic reaction (units:  $\text{mg L}^{-1}$ ),  $t$  is the irradiation time (min),  $k$  is the reaction rate constant ( $\text{min}^{-1}$ ).

### 3.3. Possible photocatalytic mechanism

In general, hydroxyl radical ( $\cdot\text{OH}$ ), holes ( $h^+$ ) and superoxide ion radicals ( $\text{O}_2^-$ ) are usually considered as oxidative active species, which have outstanding oxidation capacity [50–52]. In this experiment, 10  $\text{mmol L}^{-1}$  isopropanol, potassium iodide and p-benzoquinone were

employed as scavengers for  $\cdot\text{OH}$ ,  $h^+$  and  $\cdot\text{O}_2^-$ , respectively. Fig. 11 reveals the rates constant of three photocatalytic degradation processes with corresponding scavengers (isopropanol  $0.0049 \text{ min}^{-1}$ , potassium iodide  $0.00768 \text{ min}^{-1}$ , p-benzoquinone  $0.00324 \text{ min}^{-1}$ ) all show distinct decline trends than that without any scavenger ( $0.01653 \text{ min}^{-1}$ ). Obviously,  $\cdot\text{OH}$ ,  $h^+$  and  $\cdot\text{O}_2^-$  have similar contributions on BPA degradation by ABC-50.

It is well-known that the  $E_{\text{CB}}$  values and  $E_{\text{VB}}$  values of  $\text{g-C}_3\text{N}_4$  are at  $-1.13$  and  $1.57 \text{ eV}$ , respectively [25,39]. However, the  $E_{\text{CB}}$  values and  $E_{\text{VB}}$  values of  $\text{AgBiO}_3$  is still a debatable issue. In this paper, the potential flat-band position ( $E_{\text{fb}}$ ) of  $\text{AgBiO}_3$  was measured by Mott–Schottky curve (Fig. 12). The positive slope of the Mott–Schottky curve indicates that  $\text{AgBiO}_3$  is a typical  $n$ -type semiconductor. By the intersection point of the tangent line and  $x$ -axis, the flat band ( $E_{\text{fb}}$ ) potential of  $\text{AgBiO}_3$  is  $0.13 \text{ V}$  vs.  $\text{Ag}/\text{AgCl}$  (equivalent to  $0.33 \text{ V}$  vs. NHE). It is generally believed the  $E_{\text{CB}}$  is positive than the  $E_{\text{fb}}$  by  $0.1 \text{ V}$  [53]. Hence, based on the estimated  $E_g$  value in Fig. 5, the  $E_{\text{CB}}$  of  $\text{AgBiO}_3$  is calculated

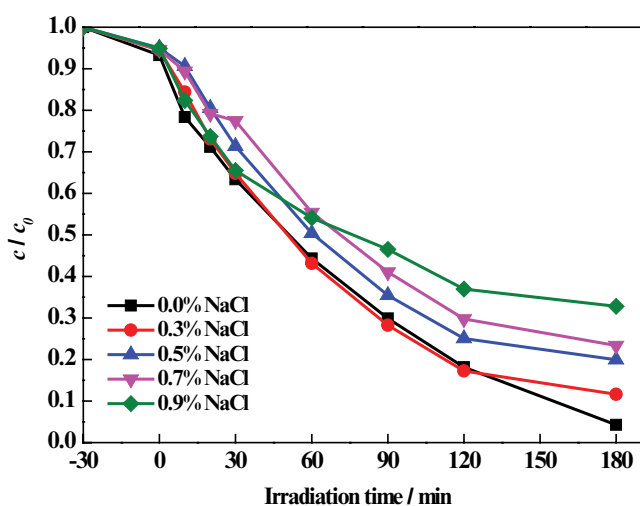


Fig. 9. Effect of the salinity on the degradation efficiency of BPA.

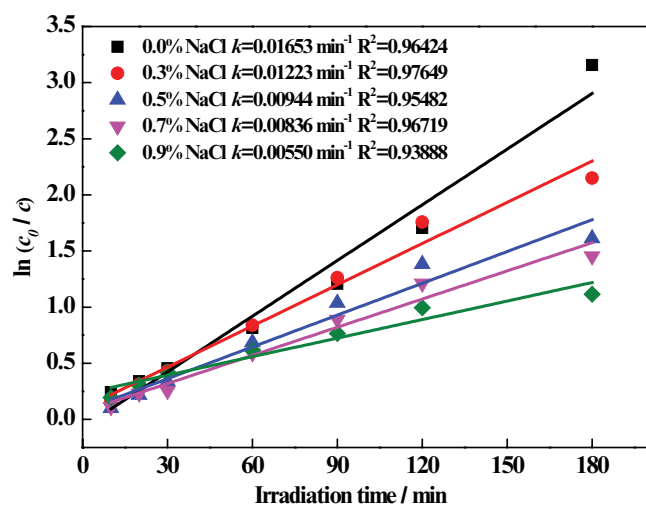


Fig. 10. The first-order kinetics simulation diagram.

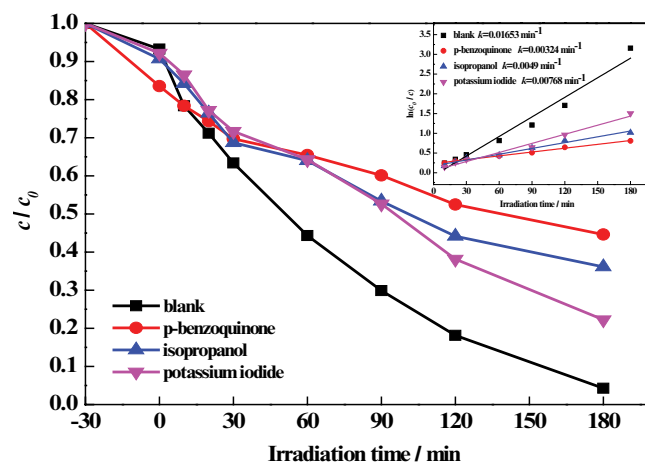


Fig. 11. Effect of trapping agents on the degradation efficiency of BPA.

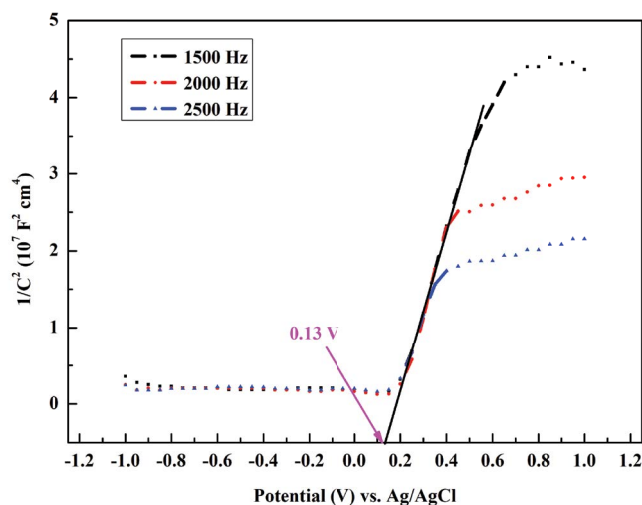


Fig. 12. Mott–Schottky curves of  $\text{AgBiO}_3$ .

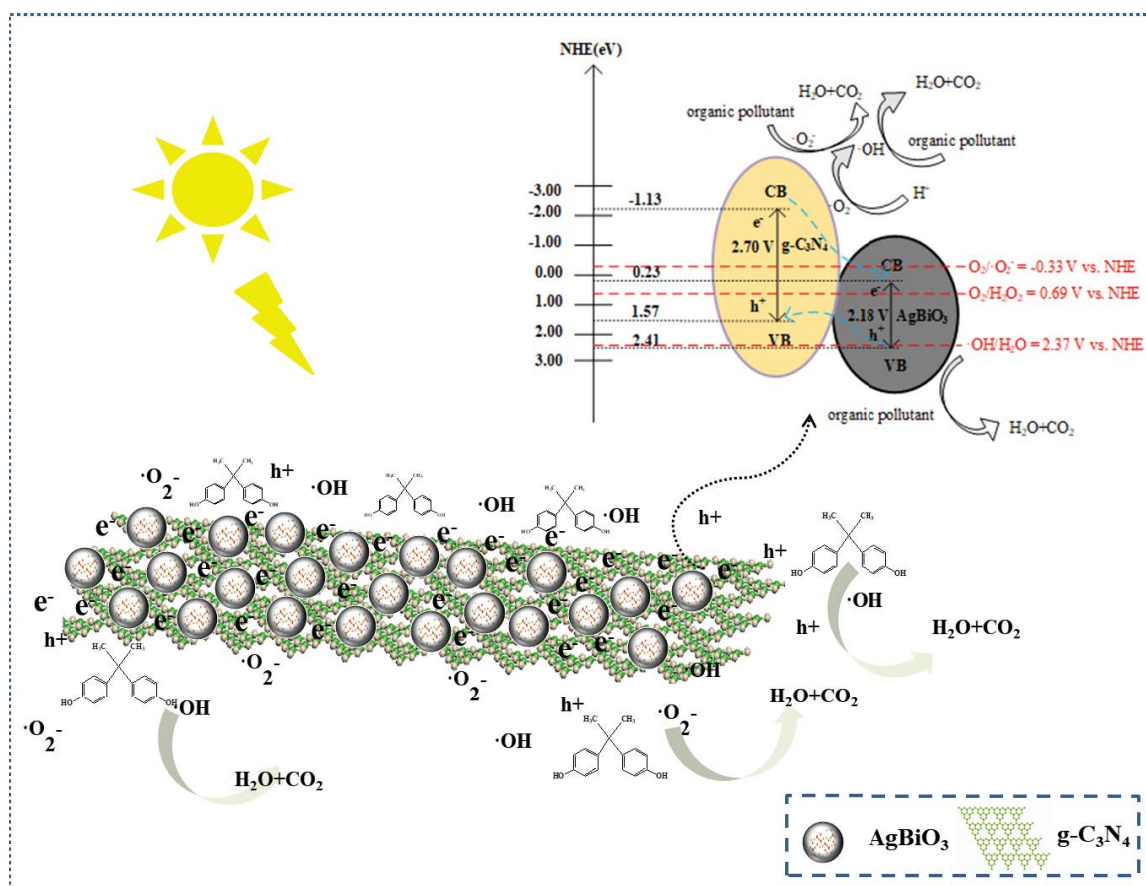


Fig. 13. Schematic drawing of the photocatalytic degradation of the ABC-50 nanocomposite.

to be 0.23 V vs. NHE and the  $E_{VB}$  of  $\text{AgBiO}_3$  is calculated to be 2.41 V.

According to the discussion above, a possible photocatalytic mechanism for ABC-50 binary nanocomposite can be predicted based on the energy band theory. Both the photo-induced electrons of  $\text{g-C}_3\text{N}_4$  and  $\text{AgBiO}_3$  could be excited from the VB to the corresponding CB under visible light irradiation. Because the CB potential of  $\text{g-C}_3\text{N}_4$  is more negative than that of  $\text{AgBiO}_3$ , the electrons ( $e^-$ ) in the CB of  $\text{g-C}_3\text{N}_4$  could be partially migrated to the CB of  $\text{AgBiO}_3$ , while the  $h^+$  can transfer from  $\text{AgBiO}_3$  to  $\text{g-C}_3\text{N}_4$  [17]. Some  $e^-$  in the CB of  $\text{AgBiO}_3$  would recombine with the  $h^+$  in the VB of  $\text{g-C}_3\text{N}_4$  owing to the relatively short distance between the VB of  $\text{g-C}_3\text{N}_4$  and the CB of  $\text{AgBiO}_3$  [21]. Moreover, the electrons in  $\text{g-C}_3\text{N}_4$  could react with dissolved  $\text{O}_2$  to generate  $\cdot\text{O}_2^-$  because the  $E_{CB}$  of  $\text{g-C}_3\text{N}_4$  is more negative than the potential of  $\text{O}_2/\text{O}_2^-$  ( $\text{O}_2/\text{O}_2^- = -0.33$  V vs. NHE) [50]. Then,  $\text{O}_2^-$  could react with  $\text{H}^+$  to produce  $\text{H}_2\text{O}_2$  ( $\text{O}_2/\text{H}_2\text{O}_2 = 0.69$  V vs. NHE) [29] and the  $\text{H}_2\text{O}_2$  could further react with the  $e^-$  to form  $\cdot\text{OH}$ . Since the  $E_{VB}$  of  $\text{AgBiO}_3$  is more positive than the potential of  $\cdot\text{OH}/\text{H}_2\text{O}$  ( $\cdot\text{OH}/\text{H}_2\text{O} = 2.37$  V vs. NHE) [39], the  $h^+$  can directly oxidize the target organic pollutant or react with  $\text{H}_2\text{O}$  to generate  $\cdot\text{OH}$  [54].

Combined with the discussions above, the possible photocatalytic reaction mechanism and analog diagram are proposed as shown in Eqs (3)–(8) and Fig. 13.



#### 4. Conclusion

In summary, the  $\text{AgBiO}_3/\text{g-C}_3\text{N}_4$  nanocomposites were successfully synthesized with a combination of calcination and ion exchange methods. The structural characterizations spectra were obtained by TEM, SEM/EDS, XRD, FT-IR, XPS, DRS, PL and BET analysis. The prepared  $\text{AgBiO}_3/\text{g-C}_3\text{N}_4$  composites were utilized to the degradation

of BPA. The prepared ABC-50 nanomaterial (50 wt.% AgBiO<sub>3</sub> in AgBiO<sub>3</sub>/g-C<sub>3</sub>N<sub>4</sub>) achieves the supreme photocatalytic activity with 95.75% degradation efficiency of BPA under 180 min visible-light irradiation. The photocatalytic reaction kinetics and the possible reaction mechanism were also speculated. The degradation process was verified to follow the pseudo-first-order kinetics. Active oxidizing species including O<sub>2</sub><sup>-</sup>, •OH and h<sup>+</sup> produced during the photocatalytic process all play important roles in the degradation of BPA.

### Acknowledgments

This work was financially supported by The Central Public-interest Scientific Institution Basal Research Fund (grant no. GYZX200304).

### References

- [1] A. Bhatnagar, L. Anastopoulos, Adsorptive removal of bisphenol A (BPA) from aqueous solution: a review, *Chemosphere*, 168 (2017) 885–902.
- [2] C.Y. Xiao, L.H. Wang, Q. Zhou, X.H. Huang, Hazards of bisphenol A (BPA) exposure: a systematic review of plant toxicology studies, *J. Hazard. Mater.*, 384 (2020) 121488–121500.
- [3] A. Tandon, S.J. Singh, M. Gupta, N. Singh, J. Shankar, N. Arjaria, S. Goyal, R.K. Chaturvedi, Notch pathway up-regulation via curcumin mitigates bisphenol-A (BPA) induced alterations in hippocampal oligodendrogenesis, *J. Hazard. Mater.*, 392 (2020) 122052–122074.
- [4] E.T. Mohammed, K.S. Hashem, A.E. Ahmed, M.T. Aly, L. Aleya, M.M. Abdel-Daim, Ginger extract ameliorates bisphenol A (BPA)-induced disruption in thyroid hormones synthesis and metabolism: involvement of Nrf-2/HO-1 pathway, *Sci. Total Environ.*, 703 (2020) 134664–134674.
- [5] R. Bahmani, D.G. Kim, M. Modareszadeh, A.J. Thompson, J.H. Park, H.H. Yoo, S. Hwang, The mechanism of root growth inhibition by the endocrine disruptor bisphenol A (BPA), *Environ. Pollut.*, 257 (2020) 113516–113528.
- [6] Y.W. Li, Q.W. Chai, J.M. Li, F. Liu, Y.Q. Wang, C.C. Zhao, Adsorption of bisphenol A (BPA) from aqueous solution onto mesoporous carbon and Fe-modified mesoporous carbon, *Desal. Water Treat.*, 150 (2019) 237–251.
- [7] F.M. Mpatani, A.A. Aryee, A.N. Kani, Q.H. Guo, E. Dovi, L.B. Qu, Z.H. Li, R.P. Han, Uptake of micropollutant-bisphenol A, methylene blue and neutral red onto a novel bagasse-b-cyclodextrin polymer by adsorption process, *Chemosphere*, 259 (2020) 127439–127451.
- [8] R. Das, G.Y. Li, B.X. Mai, T.C. An, Spore cells from BPA degrading bacteria *Bacillus* sp. GZB displaying high laccase activity and stability for BPA degradation, *Sci. Total Environ.*, 640–641 (2018) 798–806.
- [9] J.K. Xiong, T.C. An, G.Y. Li, P.A. Peng, Accelerated biodegradation of BPA in water-sediment microcosms with *Bacillus* sp. GZB and the associated bacterial community structure, *Chemosphere*, 184 (2017) 120–126.
- [10] Y. Li, T. Yang, S.H. Qiu, W.Q. Lin, J.T. Yan, S.S. Fan, Q. Zhou, Uniform N-coordinated single-atomic iron sites dispersed in porous carbon framework to activate PMS for efficient BPA degradation via high-valent iron-oxo species, *Chem. Eng. J.*, 389 (2020) 124382–124391.
- [11] P.J. He, Z. Zheng, H. Zhang, L.M. Shao, Q.Y. Tang, PAEs and BPA removal in landfill leachate with Fenton process and its relationship with leachate DOM composition, *Sci. Total Environ.*, 407 (2009) 4928–4933.
- [12] Y.F. Li, M.H. Zhou, B. Cheng, Y. Shao, Recent advances in g-C<sub>3</sub>N<sub>4</sub>-based heterojunction photocatalysts, *J. Mater. Sci. Technol.*, 56 (2020) 1–17.
- [13] S.K. Ray, J. Hur, Surface modifications, perspectives, and challenges of scheelite metal molybdate photocatalysts for removal of organic pollutants in wastewater, *Ceram. Int.*, 46 (2020) 20608–20622.
- [14] M. Pirhashemia, A.H. Yangjeh, S.R. Pouran, Review on the criteria anticipated for the fabrication of highly efficient ZnO-based visible-light-driven photocatalysts, *J. Ind. Eng. Chem.*, 62 (2018) 1–25.
- [15] M.S. Gohari, A.H. Yangjeh, M. Abitorabi, A. Rouhi, Magnetically separable nanocomposites based on ZnO and their applications in photocatalytic processes: a review, *Crit. Rev. Env. Sci. Technol.*, 48 (2018) 806–857.
- [16] A. Akhundi, A.H. Yangjeh, M. Abitorabi, S.R. Pouran, Review on photocatalytic conversion of carbon dioxide to value-added compounds and renewable fuels by graphitic carbon nitride-based photocatalysts, *Catal. Rev. Sci. Eng.*, 61 (2019) 595–628.
- [17] N. Kumaresan, M.M.A. Sinthiya, M. Sarathbavan, K. Ramamurthi, K. Sethuraman, R.R. Babuc, Synergetic effect of g-C<sub>3</sub>N<sub>4</sub>/ZnO binary nanocomposites heterojunction on improving charge carrier separation through 2D/1D nanostructures for effective photocatalytic activity under the sunlight irradiation, *Sep. Purif. Technol.*, 244 (2020) 116356–116366.
- [18] Y.L. Lan, Z.S. Li, D.H. Li, W.Y. Xie, G.X. Yan, S.H. Guo, Visible-light responsive Z-scheme Bi@β-Bi<sub>2</sub>O<sub>3</sub>/g-C<sub>3</sub>N<sub>4</sub> heterojunction for efficient photocatalytic degradation of 2,3-dihydroxynaphthalene, *Chem. Eng. J.*, 392 (2020) 123686–123696.
- [19] M.S. Nasir, G.R. Yang, I. Ayub, S.L. Wang, W. Yan, Tin diselenide a stable co-catalyst coupled with branched TiO<sub>2</sub> fiber and g-C<sub>3</sub>N<sub>4</sub> quantum dots for photocatalytic hydrogen evolution, *Appl. Catal., B*, 270 (2020) 118900–118910.
- [20] A. Akhundi, A. Badiei, G.M. Ziarani, A. Habibi-Yangjeh, M.J. Muñoz-Batista, R. Luque, Graphitic carbon nitride-based photocatalysts: toward efficient organic transformation for value-added chemicals production, *Mol. Catal.*, 488 (2020) 110902–110915.
- [21] S.L. Prabavathi, K. Govindan, K. Saravanakumar, A. Jang, V. Muthuraj, Construction of heterostructure CoWO<sub>4</sub>/g-C<sub>3</sub>N<sub>4</sub> nanocomposite as an efficient visible-light photocatalyst for norfloxacin degradation, *J. Ind. Eng. Chem.*, 80 (2019) 558–567.
- [22] G.H. Liu, M.L. Liao, Z.H. Zhang, H.Y. Wang, D.H. Chen, Y.J. Feng, Enhanced photodegradation performance of Rhodamine B with g-C<sub>3</sub>N<sub>4</sub> modified by carbon nanotubes, *Sep. Purif. Technol.*, 244 (2020) 116618–116624.
- [23] E.V. Kermani, A.H. Yangjeh, S. Ghosh, Visible-light-induced nitrogen photofixation ability of g-C<sub>3</sub>N<sub>4</sub> nanosheets decorated with MgO nanoparticles, *J. Ind. Eng. Chem.*, 84 (2020) 185–195.
- [24] X.Y. Hu, X.K. Zeng, Y. Liu, J. Lu, S. Yuan, Y.C. Yin, J. Hu, D.T. McCarthy, X.W. Zhang, Nano-layer based 1T-rich MoS<sub>2</sub>/g-C<sub>3</sub>N<sub>4</sub> co-catalyst system for enhanced photocatalytic and photoelectrochemical activity, *Appl. Catal., B*, 268 (2020) 118466–118474.
- [25] J. Mei, D.P. Zhang, N. Li, M.X. Zhang, X.Y. Gu, S.C. Miao, S.H. Cui, J. Yang, The synthesis of Ag<sub>3</sub>PO<sub>4</sub>/g-C<sub>3</sub>N<sub>4</sub> nanocomposites and the application in the photocatalytic degradation of bisphenol A under visible light irradiation, *J. Alloys Compd.*, 749 (2018) 715–723.
- [26] E.V. Kermani, A.H. Yangjeh, H.D. Khalilabad, S. Ghosh, Nitrogen photofixation ability of g-C<sub>3</sub>N<sub>4</sub> nanosheets/Bi<sub>2</sub>MoO<sub>6</sub> heterojunction photocatalyst under visible-light illumination, *J. Colloid Interface Sci.*, 563 (2020) 81–91.
- [27] J.T. Cao, X.L. Fu, L.Z. Zhao, S.H. Ma, Y.M. Liu, Highly efficient resonance energy transfer in g-C<sub>3</sub>N<sub>4</sub>-Ag nanostructure: proof-of-concept toward sensitive split-type electrochemiluminescence immunoassay, *Sens. Actuators, B*, 311 (2020) 127926–127932.
- [28] M.M. Wang, M.K. Zhang, J.L. Zhu, J. Wang, L.P. Hu, T.M. Sun, M. Wang, Y.F. Tang, g-C<sub>3</sub>N<sub>4</sub>/Co nanohybrids for ultra-sensitive simultaneous detection of uric acid and dopamine, *ChemElectroChem*, 7 (2020) 1373–1377.
- [29] J.X. Huang, D.G. Li, Y. Liu, R.B. Li, P. Chen, H.J. Liu, W.Y. Lv, G.G. Liu, Y.P. Feng, Ultrathin Ag<sub>2</sub>WO<sub>4</sub>-coated P-doped g-C<sub>3</sub>N<sub>4</sub> nanosheets with remarkable photocatalytic performance for indomethacin degradation, *J. Hazard. Mater.*, 392 (2020) 122355–122367.

- [30] M. Ghashghae, Z. Azizi, M. Ghambarian, Conductivity tuning of charged triazine and heptazine graphitic carbon nitride ( $g\text{-C}_3\text{N}_4$ ) quantum dots via nonmetal (B, O, S, P) doping: DFT calculations, *J. Phys. Chem. Solids*, 141 (2020) 109422–109427.
- [31] N.N. Zhang, L. Wen, J.Y. Yan, Y. Liu, Dye-sensitized graphitic carbon nitride ( $g\text{-C}_3\text{N}_4$ ) for photocatalysis: a brief review, *Chem. Pap.*, 74 (2020) 389–406.
- [32] Y.H. Qi, J.X. Xu, M.J. Zhang, H.F. Lin, L. Wang, In situ metaleorganic framework-derived c-doped  $\text{Ni}_3\text{S}_4/\text{Ni}_2\text{P}$  hybrid co-catalysts for photocatalytic  $\text{H}_2$  production over  $g\text{-C}_3\text{N}_4$  via dye sensitization, *Int. J. Hydrogen Energy*, 44 (2019) 16336–16347.
- [33] J.Y. Gong, C.S. Lee, E.J. Kim, J.H. Kim, W. Lee, Y.S. Chang, Self-generation of reactive oxygen species on crystalline  $\text{AgBiO}_3$  for the oxidative remediation of organic pollutants, *ACS Appl. Mater. Interfaces*, 9 (2017) 28426–28432.
- [34] R. Ramachandran, M. Sathiya, K. Ramesha, A.S. Prakash, G. Madras, A.K. Shukl, Photocatalytic properties of  $\text{KBiO}_3$  and  $\text{LiBiO}_3$  with tunnel structures, *J. Chem. Sci.*, 123 (2011) 517–524.
- [35] T. Takei, R. Haramoto, Q. Dong, N. Kumada, Y. Yonesaki, N. Kinomura, T. Mano, S. Nishimoto, Y. Kameshima, M. Miyake, Photocatalytic activities of various pentavalent bismuthates under visible light irradiation, *J. Solid State Chem.*, 184 (2011) 2017–2022.
- [36] X.Y. Yue, X.L. Miao, X.P. Shen, Z.Y. Ji, H. Zhou, Y.M. Sun, K.Q. Xu, G.X. Zhu, L.R. Kong, Q.R. Chen, N. Li, X.M. He, Flower-like silver bismuthate supported on nitrogen-doped carbon dots modified graphene oxide sheets with excellent degradation activity for organic pollutants, *J. Colloid Interface Sci.*, 540 (2019) 167–176.
- [37] X.J. Yu, J.Y. Zhou, Z.P. Wang, W.M. Cai, Preparation of visible light-responsive  $\text{AgBiO}_3$  bactericide and its control effect on the *Microcystis aeruginosa*, *J. Photochem. Photobiol.*, B, 101 (2010) 265–270.
- [38] B. Boruah, R. Gupta, J.M. Modak, G. Madras, Novel insights into the properties of  $\text{AgBiO}_3$  photocatalyst and its application in immobilized state for 4-nitrophenol degradation and bacteria inactivation, *J. Photochem. Photobiol.*, A, 373 (2019) 105–115.
- [39] D.P. Zhang, S.H. Cui, J. Yang, Preparation of  $\text{Ag}_2\text{O}/g\text{-C}_3\text{N}_4/\text{Fe}_3\text{O}_4$  composites and the application in the photocatalytic degradation of Rhodamine B under visible light, *J. Alloys Compd.*, 708 (2017) 1141–1149.
- [40] X.J. Hou, L.X. Cui, H.W. Du, L.N. Gu, Z.J. Li, Y.P. Yuan, Lowering the schottky barrier of  $g\text{-C}_3\text{N}_4/\text{Carbon}$  graphite heterostructure by N-doping for increased photocatalytic hydrogen generation, *Appl. Catal.*, B, 278 (2020) 119253–119259.
- [41] W.D. Wu, C. Xu, X.X. Shi, J. Zhao, X.X. An, H.W. Ma, Y.Y. Tian, H.F. Zhou, Effective degradation of organic pollutants and reaction mechanism with flower-like  $\text{AgBiO}_3/g\text{-C}_3\text{N}_4$  composite, *Colloids Surf.*, A, 599 (2020) 124901–124910.
- [42] H.P. Li, Z. Wang, Y.X. Lu, S. Liu, X.J. Chen, G.Y. Wei, G. Ye, J. Chen, Microplasma electrochemistry (MIPEC) methods for improving the photocatalytic performance of  $g\text{-C}_3\text{N}_4$  in degradation of RhB, *Appl. Surf. Sci.*, 531 (2020) 147307–147314.
- [43] A. Kumar, M. Khan, J.H. He, I.M.C. Lo, Visible-light-driven magnetically recyclable terephthalic acid functionalized  $g\text{-C}_3\text{N}_4/\text{TiO}_2$  heterojunction nanophotocatalyst for enhanced degradation of PPCPs, *Appl. Catal.*, B, 270 (2020) 118898–118909.
- [44] V. Dimitrov, T. Komatsu, Classification of simple oxides: a polarizability approach, *J. Solid State Chem.*, 163 (2002) 100–112.
- [45] F.E. López-Suárez, A. Bueno-López, M.J. Illan-Gomez, A. Adamski, B. Ura, J. Trawczynski, Copper catalysts for soot oxidation: alumina versus perovskite supports, *Environ. Sci. Technol.*, 42 (2008) 7670–7675.
- [46] K. Yu, S.G. Yang, S.A. Boyd, H.Z. Chen, C. Sun, Efficient degradation of organic dyes by  $\text{BiAg}_x\text{O}_y$ , *J. Hazard. Mater.*, 197 (2011) 88–96.
- [47] Z.J. Ma, K.C. Wu, B.Z. Sun, C. He, Band engineering of  $\text{AgSb}_{1-x}\text{Bi}_x\text{O}_3$  for photocatalytic water oxidation under visible light, *J. Mater. Chem. A*, 3 (2015) 8466–8474.
- [48] Q.Y. Rong, D.P. Zhang, Y. Li, Z.X. Zha, X.X. Geng, S.H. Cui, J. Yang, Synthesis of  $\text{Bi}_2\text{MoO}_7/\text{Bi}_2\text{Ti}_2\text{O}_7$  Z-scheme heterojunction as efficient visible-light photocatalyst for the glycolic acid degradation, *J. Nanosci. Nanotechnol.*, 19 (2019) 7635–7644.
- [49] H. Sudrajat, S. Babel, A new, cost-effective solar photoactive system  $\text{N-ZnO@polyester}$  fabric for degradation of recalcitrant compound in a continuous flow reactor, *Mater. Res. Bull.*, 83 (2016) 369–378.
- [50] X.S. Zhao, Y.Y. You, S.B. Huang, Y.X. Wu, Y.Y. Ma, G. Zhang, Z.H. Zhang, Z-scheme photocatalytic production of hydrogen peroxide over  $\text{Bi}_4\text{O}_5\text{Br}_2/g\text{-C}_3\text{N}_4$  heterostructure under visible light, *Appl. Catal.*, B, 278 (2020) 119251–119261.
- [51] H. Zhang, G.G. Tang, X. Wan, J. Xu, H. Tang, High-efficiency all-solid-state Z-scheme  $\text{Ag}_3\text{PO}_4/g\text{-C}_3\text{N}_4/\text{MoSe}_2$  photocatalyst with boosted visible-light photocatalytic performance for antibiotic elimination, *Appl. Surf. Sci.*, 530 (2020) 147234–147243.
- [52] C.Y. Jin, M. Wang, Z.L. Li, J. Kang, Y. Zhao, J. Han, Z.M. Wu, Two dimensional  $\text{Co}_3\text{O}_4/g\text{-C}_3\text{N}_4$  Z-scheme heterojunction: mechanism insight into enhanced peroxymonosulfate-mediated visible light photocatalytic performance, *Chem. Eng. J.*, 398 (2020) 125569–125582.
- [53] Y. Li, X.N. Zheng, J. Yang, Z.H. Zhao, S.H. Cui, Enhanced photocatalytic degradation of 2,4,6-trichlorophenol and RhB with RhB-sensitized  $\text{BiOClBr}$  catalyst based on response surface methodology, *J. Taiwan Inst. Chem. Eng.*, 119 (2021) 213–223.
- [54] M. Faisal, M. Jalalah, F.A. Harraz, A.M. El-Toni, A. Khan, Au nanoparticles-doped  $g\text{-C}_3\text{N}_4$  nanocomposites for enhanced photocatalytic performance under visible light illumination, *Ceram. Int.*, 46 (2020) 22090–22101.